

Weak coupling of acoustic-like phonons and magnon dynamics in incommensurate spin ladder compound $\text{Sr}_{14}\text{Cu}_{24}\text{O}_{41}$

Xi Chen,¹ Dipanshu Bansal,² Sean Sullivan,¹ Douglas L. Abernathy,³ Jianshi Zhou,^{1,4} Olivier Delaire,^{5,2} Li Shi^{1,4,*}

¹ Materials Science and Engineering Program, Texas Materials Institute, The University of Texas at Austin, Austin, Texas 78712, USA

² Materials Science and Technology Division, Oak Ridge National Laboratory, Oak Ridge, Tennessee 37831, USA.

³ Quantum Condensed Matter Division, Oak Ridge National Laboratory, Oak Ridge, Tennessee 37831, USA.

⁴ Department of Mechanical Engineering, The University of Texas at Austin, Austin, Texas 78712, USA.

⁵ Department of Mechanical Engineering and Materials Science, Duke University, Durham, North Carolina 27708, USA.

*lishi@mail.utexas.edu

Abstract: Intriguing lattice dynamics has been predicted for aperiodic crystals that contain incommensurate sub-structures. Here we report inelastic neutron scattering measurements of phonon and magnon dispersions in $\text{Sr}_{14}\text{Cu}_{24}\text{O}_{41}$, which contains incommensurate one-dimensional (1D) chain and two-dimensional (2D) ladder substructures. Two distinct acoustic phonon-like modes are observed for atomic motions polarized along the incommensurate axis. Corresponding to the sliding motion of one sublattice against the other, these two pseudo-acoustic modes show remarkably small energy gaps of 3-5 meV, which indicate very weak interactions between the two incommensurate sublattices. The measurements also reveal steep linear magnon dispersions from the ladder sublattice. The high group velocity of this magnon branch can explain the large magnon thermal conductivity in $\text{Sr}_{14}\text{Cu}_{24}\text{O}_{41}$ crystals. In addition, the magnon specific heat is determined from the measured total specific heat and phonon

density of states, and exhibits a Schottky anomaly due to gapped magnons. These findings offer new insights into the phonon and magnon dynamics and thermal transport properties of incommensurate magnetic crystals that contain low-dimensional substructures.

I. Introduction

Incommensurate compounds consist of two or more interpenetrating sublattices with lattice periods incommensurate along one or more crystal axes. They belong to the broader class of aperiodic crystals,¹ which also include the celebrated quasicrystals.² These compounds usually show anisotropies in electronic, optical, magnetic, and thermal properties. Examples include superconducting $\text{Hg}_{3-x}\text{AsF}_6$ containing two orthogonal and nonintersecting linear chains of mercury atoms,³ intermetallic Nowotny chimney-ladder phases⁴ with potential applications in optoelectronic⁵ and thermoelectric^{6,7} devices, and $\text{Sr}_{14}\text{Cu}_{24}\text{O}_{41}$, where the CuO_2 spin chains and Cu_2O_3 two-leg spin ladders are incommensurate along the c axis. This spin ladder compound exhibits a large magnon contribution to thermal conductivity (κ_{mag}),⁸ as well as superconductivity under high pressure when doped with Ca.⁹

Because of its relevance to not only the thermal properties but also electronic, optical, and magnetic properties via coupling between different energy excitations,¹⁰ the unusual lattice dynamics of incommensurate compounds have been investigated in a few theoretical studies over the past 40 years.¹¹⁻¹⁵ If the interaction between two incommensurate sublattices is sufficiently weak, the free energy of the system remains invariant during rigid displacement of one sublattice relative to the other along the

incommensurate axis.¹² Consequently, in the long wavelength limit, it does not cost any potential energy for relative sliding motions of the two sublattices along the incommensurate direction. This effect can also be interpreted as the softening of an optical branch in an incommensurate structure. Therefore, instead of the three acoustic modes of conventional crystals, structures with incommensurability along one axis have been predicted to exhibit four acoustic modes.^{12, 13} Two of them are acoustic sublattice displacements along the incommensurate direction, while the other two modes are conventional acoustic modes with atomic motions polarized perpendicular to the incommensurate direction. The two decoupled sublattice modes are either two longitudinal acoustic (LA) for phonons propagating parallel to the incommensurate axis or two transverse acoustic (TA) modes for phonons propagating perpendicular to the incommensurate axis. The two long-wavelength sublattice modes can be combined into two other modes with zero or nearly zero energy.¹³ One represents the rigid translation of the two sublattices as a whole, whereas the other corresponds to their out-of-phase oscillations. Interactions between the two sublattices, including non-linear force constants as well as Coulomb forces between charged sublattices,¹⁴ can result in a small energy gap for the out-of-phase sliding mode, which thus becomes a very low-energy optical mode or a pseudo-acoustic mode. In this case, there are still only three pure acoustic modes for each wave vector, similar to the case for commensurate crystals.

A few experimental studies have sought to test theories of the unusual lattice dynamics in incommensurate structures.¹⁶⁻²² Recently, infrared and Raman-active phonon modes with energy as low as 1-2 meV were observed by THz time-domain, Raman, and infrared (IR) spectroscopy measurements in $\text{Sr}_{14}\text{Cu}_{24}\text{O}_{41}$.²³ These low-energy Raman and

IR-active modes were attributed to the small energy gap of the out of phase sliding motion of the two charged sublattices. However, the behaviors of these sliding modes away from the zone center have remained elusive, as previous inelastic neutron scattering (INS) studies²⁴⁻³⁰ of $\text{Sr}_{14}\text{Cu}_{24}\text{O}_{41}$ have been mainly focused on magnetic excitations rather than lattice dynamics. Furthermore, existing experimental results on other incommensurate compounds were unable to resolve some of the predicted features of the lattice dynamics of incommensurate crystals, such as additional pseudo-acoustic modes polarized parallel to the incommensurate axis for wave vectors not only parallel to, but also perpendicular to the incommensurate axis.

Here, we report time-of-flight INS measurements of both phonon and magnon dispersions in $\text{Sr}_{14}\text{Cu}_{24}\text{O}_{41}$ single crystals. Our experimental results clearly reveal the presence of two distinct pseudo-acoustic modes, for phonons propagating either parallel or perpendicular to the incommensurate axis. The small energy gaps for these pseudo-acoustic modes are resolved and quantified. Moreover, our INS measurements reveal high-energy optical phonon modes with nearly linear dispersion and high group velocities, in addition to the extremely steep magnon dispersions of the spin-ladders, already reported in prior INS studies.^{24, 29, 30} In addition, we evaluate the magnon specific heat below 300 K based on the measured total specific heat and phonon density of states (DOS). These findings shed light into the unique phonon and magnon dynamics of this incommensurate spin-ladder compound, and can lead to further insights into the thermal transport properties of incommensurate crystals in general.

II. Experimental Methods

$\text{Sr}_{14}\text{Cu}_{24}\text{O}_{41}$ single crystals were grown with a traveling solvent floating zone method.³¹ The crystal structure was verified via X-ray diffraction (XRD) on a pulverized sample. The orientation and quality of crystals were examined by back-reflection Laue XRD. The low-temperature thermal conductivity (κ) was measured with a steady-state method. The temperature dependent specific heat was measured using a Physical Properties Measurement System (Quantum Design) in the temperature (T) interval between 1.9 and 300 K.

INS measurements were conducted on both crystals and a powder sample, with the time-of-flight Wide Angular-Range Chopper Spectrometer (ARCS) at the Spallation Neutron Source at Oak Ridge National Laboratory (ORNL).³² Two $\text{Sr}_{14}\text{Cu}_{24}\text{O}_{41}$ single crystals were co-aligned to achieve a total mass of approximately 7 g. The mosaicity of the co-alignment was about 1 degree. Several incident neutron energies, $E_i = 30, 50, 150$ meV, were used to cover the wide dynamic range of low-energy pseudo-acoustic modes as well as high-energy optic phonons and magnons. The crystals were mounted inside a closed-cycle helium refrigerator with the (0KL) crystallographic plane horizontal. The crystal measurements were performed at $T = 5$ K and 140 K. In addition, the phonon DOS was measured on a powder sample at 5 K, 70 K, 140 K, 210 K and 300 K. Two incident neutron energies, $E_i = 50$ and 200 meV, were used at each temperature to achieve higher resolution at low energy and to probe the full phonon spectrum, respectively.

The data from both single crystal and powder measurements were normalized by the total incident flux and corrected for detector efficiency. Subsequently, the data were transformed from instrument coordinates, including the 2-theta and time of event, to the

physical momentum transfer, \mathbf{Q} , and energy transfer, E , using the MANTID reduction software.³³ For the powder sample, the scattering from the empty container was processed identically and subtracted from the sample measurements. The experimental phonon DOS was analyzed within the incoherent scattering approximation, and corrected for multi-phonon scattering effects.³⁴ The data nearby the elastic peak were removed in order to eliminate strong elastic signals, and a Debye-like quadratic energy dependence was used to extrapolate the phonon DOS at low energy $E < 3$ meV for $E_i = 50$ meV and $E < 8$ meV for $E_i = 200$ meV.

Two-dimensional intensity maps for the dynamical structure factor, $S(\mathbf{Q}, E)$, were obtained from slices of the four-dimensional dataset using the HORACE software.³⁵ In order to improve the appearance of these maps, a Gaussian smoothing filter was applied to the numerical data, with a standard deviation of 2 pixels and a filter size of 2×2 pixels. Miller indices are henceforth expressed as $[HKL]_C$ for the chain sublattice and $[HKL]_L$ for the ladder sublattice.

III. Results and Discussions

A. Crystal structure and thermal conductivity of $\text{Sr}_{14}\text{Cu}_{24}\text{O}_{41}$

The unit cell of $\text{Sr}_{14}\text{Cu}_{24}\text{O}_{41}$ contains two incommensurate sublattices along the c axis, which are CuO_2 chains and Cu_2O_3 two-leg ladders, as illustrated in Fig. 1(a). Planes of CuO_2 chains are stacked alternately with planes of Cu_2O_3 ladders. One-dimensional Sr chains are present between the Cu_2O_3 ladders and CuO_2 chains. The lattice parameters are $a = 11.469$ Å, $b = 13.368$ Å, and $c_L = 3.931$ Å for the ladders and $c_C = 2.749$ Å for the chains. Thus, the c axis is incommensurate for the ladder and chain sublattices,³⁶ with a ratio of approximately $\alpha = \sqrt{2} : 1$. Due to the incommensurate crystal structure, two sets

of Bragg peaks associated with the chain and ladder sublattices, respectively, are observed in the $(0KL)$ plane in the elastic scattering channel, as shown in Fig. 1(b). The ladders contribute strong peaks at $(0K-2)_L$ in their corresponding reciprocal lattice. Weaker diffraction peaks from the chains are observed at $(0K-1)_C$ and $(0K-2)_C$, equivalent to $(0K-1.43)_L$ and $(0K-2.85)_L$. Similar diffraction patterns were also observed in electron diffraction measurements on $\text{Sr}_{14}\text{Cu}_{24}\text{O}_{41}$.³⁷ The thermal conductivity measurement results of $\text{Sr}_{14}\text{Cu}_{24}\text{O}_{41}$ single crystals reported by Hess *et al.*³⁸ and those obtained in the present work are shown in Fig. 1(c). The two measurements are in good agreement and show a striking anisotropy in both the absolute value and temperature dependence of κ . The κ along c shows a broad peak at about 140 K in addition to the phonon peak at a lower temperature. This feature has been attributed to the fast-propagating magnetic excitations along the spin ladders.^{38,39} Below 40 K, the main contribution to κ comes from phonons due to the presence of large magnon gaps and high electrical resistivity.^{24,40} The lattice thermal conductivity is found to be much larger along c .

B. Phonon dispersion of $\text{Sr}_{14}\text{Cu}_{24}\text{O}_{41}$

Figure 2(a) shows the $S(\mathbf{Q}, E)$ along $\mathbf{q} = [00L]$. For a net momentum transfer from the incident neutron of $\mathbf{Q} = \mathbf{G}_{HKL} + \mathbf{q}$, the measured neutron scattering intensity increases with $|\mathbf{Q} \cdot \boldsymbol{\epsilon}_i^\alpha|^2$, where $\boldsymbol{\epsilon}_i^\alpha$ is the polarization vector of the i^{th} atom in the unit cell for a particular phonon mode α .⁴¹ Consequently, the phonon modes with strong intensity in the Brillouin zone around $\mathbf{G}_{HKL} = (00L)$ are the longitudinal modes with \mathbf{q} along $[00L]$, or the transverse modes polarized along $[00L]$ and propagating normal to it. It should be noted that the phonon intensity generally increases as $|\mathbf{Q}|^2$, while the magnon intensity vanishes

at large $|\mathbf{Q}|$ because of the magnetic form factor.⁴² As can be seen in Fig. 2(a), two separate LA-like phonon branches are clearly observed. One LA-like branch extends up to about 20 meV with a minimum energy at $(00-2)_L$ or $(00-4)_L$, indicating that this mode, referred as p-LA_L hereafter, originates from the atomic motion of the ladders polarized along the incommensurate direction. The other LA-like branch extends up to about 30 meV and reaches a minimum energy at $(00-2.85)_L$ or $(00-2)_C$, so that this mode (p-LA_C) is associated with the atomic motion of the chains. The group velocities of the very linear LA-like modes are $v_1 = 7300 \text{ m s}^{-1}$ for the chains and $v_2 = 4000 \text{ m s}^{-1}$ for the ladders, as listed in Table I. The velocities of the acoustic-like modes depend on the mass density (ρ) and the elastic constant (K) of the two sublattices as $v^2 = K/\rho$.²⁰ With a mass density $\rho_C = 1.51 \text{ g cm}^{-3}$ for the chains and $\rho_L = 3.86 \text{ g cm}^{-3}$ for the ladders, the ratio of elastic constants between chain (K_C) and ladder (K_L) sublattices is thus estimated to be $K_C : K_L = 1.24:1$. The larger elastic constant for the chain sublattice is consistent with the smaller distance between the nearest Cu atoms along the c axis for the chain sublattice (2.749 Å) as compared to that for the ladder sublattice (3.931 Å). In the low-frequency limit, the sound velocity of the LA mode associated with the global translational symmetry is given as

$$v_s = \sqrt{(m_C v_C^2 + m_L v_L^2)/(m_C + m_L)}, \quad (1)$$

where m is the unit-cell mass of either sublattice as denoted by the C or L subscript.⁴³ The obtained value is about 5200 m s^{-1} according to Eq. (1). In comparison, the longitudinal sound velocity extracted from the longitudinal elastic constant measured by an ultrasonic technique is about 6400 m s^{-1} ,⁴⁴ which falls between the two group velocity values

observed in INS measurements and is slightly higher than the above calculated value for the LA mode for the global translation of both sublattices.

A linear extrapolation of the two LA-like branches down to the (00L) zone center indicates non-zero energy gaps [Fig. 2(b)], although the energy gaps are partially obscured in Fig. 2(a) because of the strong Bragg peaks for the (00L) zones. In comparison, the presence of the energy gaps for the two LA-like modes is clearly shown by the INS data obtained at (01L) zones with forbidden Bragg peaks [Fig. 2(c)]. These energy gaps are further confirmed by the constant \mathbf{Q} scan data measured at the $\mathbf{Q} = (01-2)_L$ and $\mathbf{Q} = (01-2)_C$ zone centers for the ladder and chain sublattices, respectively, as shown in Fig. 2(d). The peaks in the Fig. 2(d) are fitted to obtain the energy gaps. The obtained gap values are ~ 5 meV for p-LA_L, and ~ 3 meV for p-LA_C, respectively, and show weak temperature dependence.

Figure 2(e) and (f) show the INS data obtained along $[H1-2]_C$ and $[H1-2]_L$. Very flat INS intensity is observed along $[H1-2]_C$ in the range of $-1.5 < H < 1.5$ with $E \approx 3$ meV. This flat and weak dispersion indicates nearly vanishing and small group velocities along a for the chain motion mainly polarized along c . In comparison, the ladder sublattice dispersion along $[H1-2]_L$ is clearly evident. The corresponding group velocities for the c -polarized TA-like modes of the two sublattices, referred as c -TA_C [Fig. 2(e)] and c -TA_L [Fig. 2(f)], are close to 0 and 3800 m s^{-1} , respectively, as listed in Table I. The local mode type character in the chain sublattice indicates that the interactions between adjacent chains are very weak and each chain vibrates individually. On the other hand, for the ladders, we observe the collective excitation from adjacent layers, indicating relatively strong interactions. In addition, the energy gap of ~ 5 meV is also observed in

the TA-like mode for $[H1-2]_L$, which is consistent with value obtained by constant Q scan in Fig. 2(d).

Based on these INS data, the two acoustic-like modes are illustrated in the schematic of Fig. 3. The chain excitation is much less dispersive along a than along c because of relatively weak inter-chain interaction compared to intra-chain interaction. The much larger group velocities along c than along a can explain the highly anisotropic lattice thermal conductivity for $\text{Sr}_{14}\text{Cu}_{24}\text{O}_{41}$ below 40 K, where phonons dominate the contribution to κ .

The observed energy gaps are caused by the long-range Coulomb interaction between the two ionic sublattices. The gap value (ω_{gap}) can be calculated as

$$\omega_{\text{gap}} = \sqrt{\frac{4\pi n_c q_c^2}{m_c} \left(1 + \frac{c_L}{c_c} \frac{m_c}{m_L}\right)}, \quad (2)$$

where n and q are the atomic mass density and charge of each sublattice as denoted by the C and L subscripts.¹⁴ This equation has been used to calculate a gap value of 3.7 meV for $\text{Sr}_{14}\text{Cu}_{24}\text{O}_{41}$ in a prior work.²³ The energy gaps obtained from the INS measurements are comparable to these calculated values, and are slightly higher than the two 1-2 meV infrared active modes observed in $\text{Sr}_{14}\text{Cu}_{24}\text{O}_{41}$ at 5 K.²³ The gap values are also larger than the value of 0.1 meV observed in $\text{Hg}_{3-x}\text{AsF}_6$.⁴⁵

The earlier INS experimental observation of additional acoustic-like modes in $\text{Hg}_{3-x}\text{AsF}_6$ stimulated the initial theoretical study of lattice dynamics of incommensurate structures.^{12, 16, 45} The theoretical studies have suggested experimental searches of new acoustic-like modes in Nowotny chimney-ladder structures such as higher manganese silicides (HMS). Recent INS measurements have indeed discovered the presence of a low

lying acoustic-like polarization associated with the twisting motion of the Si ladder sublattice relative to the Mn chimney sublattice.⁴¹ The twisting mode is observed near the Bragg peaks of the Si sublattices, with a component of the atomic motion polarized along the incommensurate direction.

Besides $\text{Hg}_{3-x}\text{AsF}_6$ and HMS, the appearance of additional acoustic-like branches along the incommensurate crystal axis has been observed in other incommensurate host-guest crystals including Rb-IV,²¹ *n*-nonadecane-urea,²² $[\text{Pt}(\text{en})_2][\text{Pt}(\text{en})_2\text{I}_2](\text{ClO}_4)_4$,⁴⁶ and layered superconducting cuprates $\text{Bi}_2\text{Sr}_2\text{CaCu}_2\text{O}_{8+\delta}$ and $\text{Bi}_2\text{Sr}_2\text{CuO}_{6+\delta}$.^{19, 20} For $\text{Bi}_2\text{Sr}_2\text{CaCu}_2\text{O}_{8+\delta}$ and $\text{Bi}_2\text{Sr}_2\text{CuO}_{6+\delta}$,^{19, 20} the triple axis INS measurements were not able to verify whether a gap is present in the long-wavelength limit for the two observed LA-like modes corresponding to the sliding motions of the two respective sublattices, and found only one instead of two TA-like modes polarized along the incommensurate axis when the wave vector is perpendicular to the incommensurate axis. Similarly, the measurement data for the other aforementioned incommensurate structures are not able to provide clear evidence of these fine features.

In comparison, the INS data in Fig. 2(f) essentially show a low-group velocity TA-like mode of the ladders for polarizations along *c* and wave vectors along *a*. This TA-like mode for the ladders is also observed in Fig. 4(a) near the $[H0-2]_{\perp}$ zone. However, this combination of atomic polarization and wave vectors for the chains yields the dispersionless INS data in Fig. 2(e), which resemble the typical behavior of optical phonons instead of acoustic phonons. In addition to these TA-like or low-lying optical modes polarized along *c*, the INS measurements reveal the TA mode polarized along *b*

for wave vectors along a [Fig. 4(b)], and low-energy optical phonon modes in the range of 7-15 meV near the $[H 16 -2]_L$ zone [Fig. 4(c)].

To search for clear experimental support of the theoretical predictions^{12, 13} of two TA-like branches polarized along the incommensurate axis, we investigate $S(\mathbf{Q}, E)$ for wave vectors propagating along b . The linear LA branch near $(0 16 0)$ spans multiple Brillouin zones and extends to about 14 meV, as shown in Fig. 5(a). For INS data near a $(00L)$ zone with large L , the data along $[0K0]$ contain mainly transverse polarizations along c . As shown in Fig. 5(b), a TA-like branch near $(002)_L$ extends to ~ 7 meV. This branch is the c -polarized TA-like branch associated with the ladders. As the INS data in Fig. 5(c) are plotted with the Miller index along the c axis of the chains $L_C = -2$, the low-energy branch up to ~ 4 meV is the TA-like branch associated with the chains. According to theoretical models of Axe and Bak,¹² two TA-like modes polarized along the incommensurate axis are expected for wave vectors perpendicular to the axis. While this feature was not reported in prior studies, it is clearly observed in Figs. 5(b,c). Furthermore, it is noted that the c -polarized TA-like mode of the ladders exhibits a larger group velocity than that of the chains, suggesting stiffer force constants inside the ladders along b than those between the chains along the same direction.

In addition to the two acoustic-like modes polarized along the c axis for wave vectors both parallel and perpendicular to c , the INS data show additional unique features for phonons polarized perpendicular to c . An acoustic mode of the ladders is observed near the $(0 16 0)$ and $(0 16 -2)_L$ zones with \mathbf{q} along $[00L]$, as displayed in Fig. 6(a). This mode is a TA phonon polarized along b with \mathbf{q} along c , and has a group velocity of 2100 m s^{-1} . Some optical phonons ranging from about 7 to 70 meV are observed in the

dispersion data measured along c , as shown in Figs. 6(b-d). A relatively low-lying optical polarization [Fig. 6(b)] exhibits a “W” shape, which is centered at $(07-2)_L$. One optical mode near $(04-2)_L$ appears in the energy range between 16 and 22 meV [Fig. 6(c)]. A unique feature of this optical branch is its nearly linear dispersion, which is equivalent to a relatively high group velocity of 1800 m s^{-1} . Another high-energy optical mode shows a maximum energy of $\sim 70 \text{ meV}$ at the Miller index along the c axis of the ladders $L_L = 3$ or 5, and bends down to 56 meV at the zone boundary with a high group velocity of 2800 m s^{-1} [Fig. 6(d)]. The high-energy optical mode should be due to the oxygen vibrations bounded to Cu because oxygen is the lightest ion and Cu-O is the shortest bond in the structure.⁴⁷ The shape of this mode is similar to the longitudinal oxygen bond-stretching mode in the CuO_2 plane observed in doped La_2CuO_4 compounds.⁴⁸ In addition, two Raman-active modes at 68 and 72 meV have been found in $\text{Sr}_{14}\text{Cu}_{24}\text{O}_{41}$,⁴⁹ which are assigned as breathing modes of oxygen atoms in the ladder, and vibrations of oxygen in the chain along the c axis, respectively. These findings reveal unique features of phonon dynamics of spin ladder compounds.

C. Magnon dispersion of $\text{Sr}_{14}\text{Cu}_{24}\text{O}_{41}$

The magnetic structure of $\text{Sr}_{14}\text{Cu}_{24}\text{O}_{41}$ also consists of two parts. In Cu_2O_3 ladders, the Cu $S=1/2$ spins are strongly coupled via the 180° Cu-O-Cu superexchange, while the magnetic interactions are weak in the array of CuO_2 $S = 1/2$ spin chains due to the 90° Cu-O-Cu configuration. In previous INS studies of $\text{Sr}_{14}\text{Cu}_{24}\text{O}_{41}$, the coupling energies for the ladders were found to be $J_{//} = 130 \text{ meV}$ along the ladder and $J_{\perp} = 72 \text{ meV}$ along the rung.²⁴ The dominant intra-dimer exchange of the chains was evaluated to

be $J \approx 10$ meV, and the inter-chain exchanges were found to be $J_{\parallel} \approx -1.1$ meV and $J_{\perp} \approx 1.7$ meV.²⁷ The microscopic origin of dimerization is suggested to be the localization of holes at low temperature on structurally modulated chains.⁵⁰ The formed super-structure on the chains has a periodicity of $5c_C$, which corresponds to dimers of two spins coupled across one hole with neighboring dimers separated by two holes.^{51, 52}

The magnon dispersion of $\text{Sr}_{14}\text{Cu}_{24}\text{O}_{41}$ along c is shown in Fig. 7(a). The stiff dispersions at $L_L = -(0.5+n)$, showing a large energy gap of ~ 31 meV, are associated with spin-triplet excitations of the ladders.²⁴ Even-leg ladders have spin-liquid ground states due to their purely short-range spin correlation.⁵³ A spin gap is formed since a finite energy is needed to create an $S = 1$ spin excitation in the ladder.⁵⁴ These excitations are particularly clearly observed at low energy, as shown in Fig. 7(b). Owing to the large bandwidth of these triplet excitations up to 200 meV, our INS measurements have only mapped out about half of the dispersion. Nevertheless, the steep dispersion indicates the large group velocity for magnons in the spin ladders, which is one reason for the high κ_{mag} observed in $\text{Sr}_{14}\text{Cu}_{24}\text{O}_{41}$ single crystals.^{38, 39} Furthermore, it is noticed that the LA-like branch of the chains nearly crosses the linear magnon dispersion of the ladders as shown in Fig. 7(a). The high energy optical modes of the ladders cross the magnon dispersion at about 55 and 72 meV as shown in Fig. 7(b). By fitting the magnon mean free path of the spin ladder compound $\text{La}_5\text{Ca}_9\text{Cu}_{24}\text{O}_{41}$ with undoped ladders based on a kinetic model, Hess *et al.* have suggested that scattering of magnons by such high energy optical phonons is the main scattering mechanism in this compound.⁵⁵

Figure 8 shows the low-energy magnon dispersions of the chains, which are weakly dispersive along the a and c axes. These low-energy magnons have also been observed in previous INS measurements.^{24, 26, 27, 29, 51} As shown in Fig. 8(a), two different dispersions have been observed, which show energy gap values of about 9 and 11 meV, respectively. These dispersions have a periodicity of $0.2 \times (2\pi/c_C)$, suggesting that they originate from the aforementioned dimerized super-structure of the chain sublattice. Our results are in agreement with the INS data reported by Matsuda *et al.*⁵¹ The energy gap of this magnon dispersion results from a dimerized state in the antiferromagnetic chains as suggested by both theoretical⁵⁶ and experimental studies.⁵¹ Figure 8(b,c) show the magnon dispersions along $[H 1 0.7]_C$ and $[H 1 0.2]_C$, respectively. One branch is shifted by one reciprocal lattice unit $2\pi/a$ with respect to the other. The position of these two magnon dispersions matches with previous INS studies.²⁷ These two magnon branches result from the spin interaction of the chains along a .^{27, 51}

D. Phonon and Magnon specific heat contributions of $\text{Sr}_{14}\text{Cu}_{24}\text{O}_{41}$

While the observed magnon dispersion is in general agreement with prior reports, this work has obtained the magnon contribution to the specific heat from the measured phonon density of states and total specific heat. Since the scattering intensity from magnons is limited to low $|\mathbf{Q}|$,⁴² we used higher $|\mathbf{Q}|$ data ($3 < |\mathbf{Q}| < 6.5 \text{ \AA}^{-1}$ for 50 meV and $7 < |\mathbf{Q}| < 12 \text{ \AA}^{-1}$ for 200 meV) to obtain the phonon DOS. Figure 9(a,b) show the temperature dependence of neutron weighted phonon DOS with $E_i = 50$ meV and 200 meV, respectively. We observe two phonon peaks with a low energy peak at ~ 30 meV and a high energy peak at 70 meV. The phonon cutoff energy is about 90 meV, in

agreement with INS phonon dispersion results. With the increase of temperature, a slight softening of phonon is observed. The phonon DOS measured at 5 K was used to calculate the phonon specific heat (C_p) of $\text{Sr}_{14}\text{Cu}_{24}\text{O}_{41}$ according to

$$C_p(T) = 3k_B \frac{N}{\rho V} \int x^2 \frac{\exp(x)}{(\exp(x) - 1)^2} g(\omega) d\omega, \quad (3)$$

where $x = \hbar\omega/k_B T$, k_B is Boltzmann constant, ω is the angular frequency of phonons, N is the number of atoms in a unit cell, V is the volume of the unit cell, and $g(\omega)$ is phonon DOS. For energy below 40 meV, $g(\omega)$ was obtained from the phonon DOS measured with $E_i = 50$ meV; while $g(\omega)$ above 40 meV is from the phonon DOS measured with $E_i = 200$ meV. As shown in Fig. 9(c), a bump between 10 K and 75 K is observed in the $C_{p,\text{Exp}}$ data but not in the $C_{p,\text{Calc}}$ in the $C_p(T)/T^3$ plot. This discrepancy is due to the contribution of magnons to the total measured $C_{p,\text{Exp}}$. Figure 9(d) shows the difference between the measured C_p and calculated C_p . A low energy peak at about 100 K is observed, akin to a Schottky contribution from the gapped magnon dispersions. This peak temperature is comparable to the low-energy magnon gap, about 90 K. The magnon contribution is about $0.03 \text{ J g}^{-1} \text{ K}^{-2}$ at 300 K, about 7% of the total specific heat, which is of the same order of magnitude of the calculated C_p of spin ladder compound $\text{Ca}_9\text{La}_5\text{Cu}_{24}\text{O}_{41}$.⁵⁷ At $T = 100$ K, the magnon specific heat is found to be about 15% of the total C_p .

IV. Conclusions

INS measurements of the spin ladder compound $\text{Sr}_{14}\text{Cu}_{24}\text{O}_{41}$ clearly show the presence of two weakly coupled LA-like modes, emerging from the ladder and chain sublattices, respectively, along the incommensurate c axis. These two LA-like modes exhibit small energy gaps of 3-5 meV due to the weak interaction between the two sublattices. Moreover, our measurements also reveal two decoupled c -polarized TA-like modes associated with the two sublattices for wave vectors perpendicular to the incommensurate axis. This latter feature provides further experimental support of prior theoretical predictions of the lattice dynamics of incommensurate compounds. A number of optical phonons are present in the energy ranging from 5-70 meV, some of which show relatively high group velocities. In addition, the steep magnon dispersion of the ladder sublattice has been mapped out from 31 to 120 meV. The high group velocity of these ladder-derived magnons is likely responsible for the high κ_{mag} in $\text{Sr}_{14}\text{Cu}_{24}\text{O}_{41}$. The magnon contribution to the specific heat has been evaluated from the measured C_p and phonon DOS. A Schottky anomaly has been found in the calculated magnon specific heat, which is due to the gapped magnon dispersions. At $T = 100$ K, magnons can contribute to $\sim 15\%$ of the total specific heat. These findings provide new insights into the phonon and magnon dynamics in incommensurate compounds, and may enable further theoretical analysis to explain these observations. Moreover, two-dimensional (2D) van der Waals heterostructures,⁵⁸⁻⁶¹ which are being actively investigated, are essentially incommensurate crystals, and can potentially exhibit similar phonon dynamics features as those observed here for the spin ladder compounds, which consist of weakly coupled low-dimensional substructures.

Acknowledgements

This work was supported by US Army Research Office (ARO) MURI award W911NF-14-1-0016. Neutron scattering measurements and analysis (D.B. and O.D.) were supported by the U.S. Department of Energy, Office of Science, Basic Energy Sciences, Materials Sciences and Engineering Division, through the Office of Science Early Career Research Program. The use of Oak Ridge National Laboratory's Spallation Neutron Source was sponsored by the Scientific User Facilities Division, Office of Basic Energy Sciences, U.S. Department of Energy. The authors thank helpful discussion with David G. Cahill and Yaroslav Tserkovnyak.

References

- 1 G. Chapuis and A. Arakcheeva, *Rend. Fis. Acc. Lincei* **24**, S77 (2013).
- 2 D. Levine and P. J. Steinhardt, *Phys. Rev. Lett.* **53**, 2477 (1984).
- 3 I. D. Brown, B. D. Cutforth, C. G. Davies, R. J. Gillespie, P. R. Ireland, and J. E. Vekris, *Can. J. Chem.* **52**, 791 (1974).
- 4 H. Nowotny, *The Chemistry of Extended Defects in Non-Metallic Solids* (North-Holland Publishing Co. Amsterdam, 1970).
- 5 J. E. Mahan, *Thin Solid Films* **461**, 152 (2004).
- 6 I. Kawasumi, M. Sakata, I. Nishida, and K. Masumoto, *J. Mater. Sci.* **16**, 355 (1981).
- 7 X. Chen, S. N. Girard, F. Meng, E. Lara-Curzio, S. Jin, J. B. Goodenough, J. S. Zhou, and L. Shi, *Adv. Energy Mater.* **4**, 1400452 (2014).
- 8 A. V. Sologubenko, K. Gianno, H. R. Ott, U. Ammerahl, and A. Revcolevschi, *Phys. Rev. Lett.* **84**, 2714 (2000).
- 9 M. Uehara, T. Nagata, J. Akimitsu, H. Takahashi, N. Mōri, and K. Kinoshita, *J. Phys. Soc. Jpn* **65**, 2764 (1996).
- 10 G. T. Hohensee, R. B. Wilson, J. P. Feser, and D. G. Cahill, *Phys. Rev. B* **89** (2014).
- 11 G. Theodorou and T. M. Rice, *Phys. Rev. B* **18**, 2840 (1978).
- 12 J. D. Axe and P. Bak, *Phys. Rev. B* **26**, 4963 (1982).
- 13 W. Finger and T. M. Rice, *Phys. Rev. B* **28**, 340 (1983).
- 14 G. Theodorou, *Solid State Commun.* **33**, 561 (1980).
- 15 R. Currat, E. Kats, and I. Luk'yanchuk, *Eur. Phys. J. B* **26**, 339 (2002).
- 16 J. M. Hastings, J. P. Pouget, G. Shirane, A. J. Heeger, N. D. Miro, and A. G. MacDiarmid, *Phys. Rev. Lett.* **39**, 1484 (1977).
- 17 A. J. Schultz, J. M. Williams, N. D. Miro, A. G. Macdiarmid, and A. J. Heeger, *Inorg. Chem.* **17**, 646 (1978).
- 18 I. Heilmann, J. Axe, J. Hastings, G. Shirane, A. Heeger, and A. MacDiarmid, *Phys. Rev. B* **20**, 751 (1979).
- 19 J. Etrillard, P. Bourges, H. He, B. Keimer, B. Liang, and C. Lin, *Europhys. Lett.* **55**, 201 (2001).
- 20 J. Etrillard, L. Bourgeois, P. Bourges, B. Liang, C. Lin, and B. Keimer, *Europhys. Lett.* **66**, 246 (2004).
- 21 I. Loa, L. Lundegaard, M. McMahon, S. Evans, A. Bossak, and M. Krisch, *Phys. Rev. Lett.* **99**, 035501 (2007).

- 22 B. Toudic, R. Lefort, C. Ecolivet, L. Guérin, R. Currat, P. Bourges, and T. Brezczewski,
Phys. Rev. Lett. **107**, 205502 (2011).
- 23 V. K. Thorsmølle, C. C. Homes, A. Gozar, G. Blumberg, J. L. M. van Mechelen, A. B.
Kuzmenko, S. Vanishri, C. Marin, and H. M. Rønnow, Phys. Rev. Lett. **108**, 217401
(2012).
- 24 R. S. Eccleston, M. Uehara, J. Akimitsu, H. Eisaki, N. Motoyama, and S.-i. Uchida, Phys.
Rev. Lett. **81**, 1702 (1998).
- 25 M. Matsuda, et al., Phys. Rev. B **56**, 14499 (1997).
- 26 M. Matsuda, K. Katsumata, H. Eisaki, N. Motoyama, S. Uchida, S. Shapiro, and G.
Shirane, Phys. Rev. B **54**, 12199 (1996).
- 27 L. Regnault, J. Boucher, H. Moudden, J. Lorenzo, A. Hiess, U. Ammerahl, G. Dhahlenne,
and A. Revcolevschi, Phys. Rev. B **59**, 1055 (1999).
- 28 M. Matsuda, T. Yosihama, K. Kakurai, and G. Shirane, Phys. Rev. B **59**, 1060 (1999).
- 29 J. E. Lorenzo, L. P. Regnault, C. Boullier, N. Martin, A. H. Moudden, S. Vanishri, C.
Marin, and A. Revcolevschi, Phys. Rev. Lett. **105** (2010).
- 30 G. Deng, N. Tsyrlin, P. Bourges, D. Lamago, H. Rønnow, M. Kenzelmann, S. Danilkin,
E. Pomjakushina, and K. Conder, Phys. Rev. B **88** (2013).
- 31 A. Revcolevschi, U. Ammerahl, and G. Dhahlenne, J. Cryst. Growth **198–199, Part 1**, 593
(1999).
- 32 D. L. Abernathy, M. B. Stone, M. J. Loguillo, M. S. Lucas, O. Delaire, X. Tang, J. Y. Y.
Lin, and B. Fultz, Rev. Sci. Instrum. **83**, 015114 (2012).
- 33 O. Arnold, et al., Nucl. Instrum. Meth. A **764**, 156 (2014).
- 34 B. Fultz, T. Kelley, M. Mckerns, J. Lee, O. Delaire, and M. Kresch, Experimental
Inelastic Neutron Scattering: Introduction to DANSE
<http://citeseerx.ist.psu.edu/viewdoc/download?doi=10.1.1.176.2866&rep=rep1&type=pdf>
- 35 J. Ma, et al., Nat. Nanotechnol. **8**, 445 (2013).
- 36 T. Vuletić, B. Korin-Hamzić, T. Ivek, S. Tomić, B. Gorshunov, M. Dressel, and J.
Akimitsu, Phys. Rep. **428**, 169 (2006).
- 37 J. Wang, Y. Lin, H. Zou, S. Pu, and J. Shi, J. Phys. Condens. Matter **21**, 075601 (2009).
- 38 C. Hess, C. Baumann, U. Ammerahl, B. Büchner, F. Heidrich-Meisner, W. Brenig, and
A. Revcolevschi, Phys. Rev. B **64**, 184305 (2001).
- 39 A. Sologubenko, K. Gianno, H. Ott, U. Ammerahl, and A. Revcolevschi, Phys. Rev. Lett.
84, 2714 (2000).
- 40 N. Motoyama, T. Osafune, T. Kakeshita, H. Eisaki, and S. Uchida, Phys. Rev. B **55**,
R3386 (1997).
- 41 X. Chen, et al., Nat. Commun. **6**, 6723 (2015).
- 42 H. U. Guedel, A. Stebler, and A. Furrer, Inorg. Chem. **18**, 1021 (1979).
- 43 W. Finger and T. Rice, Phys. Rev. B **28**, 340 (1983).
- 44 D. König, et al., Physica B Condens. Matter **237**, 117 (1997).
- 45 I. U. Heilmann, J. M. Hastings, G. Shirane, A. J. Heeger, and A. G. MacDiarmid, Solid
State Commun. **29**, 469 (1979).
- 46 J. F. Bardeau, A. Bulou, B. I. Swanson, and B. Hennion, Phys. Rev. B **58**, 2614 (1998).
- 47 N. Ogita, Y. Sakaguchi, Y. Fujino, T. Nagata, J. Akimitsu, and M. Udagawa, Physica B
Condens. Matter **281**, 955 (2000).
- 48 R. J. McQueeney, Y. Petrov, T. Egami, M. Yethiraj, G. Shirane, and Y. Endoh, Phys.
Rev. Lett. **82**, 628 (1999).
- 49 Z. Popović, M. Konstantinović, V. Ivanov, O. Khuong, R. Gajić, A. Vietkin, and V.
Moshchalkov, Phys. Rev. B **62**, 4963 (2000).
- 50 Z. Hiroi, S. Amelinckx, G. VanTendelo, and N. Kobayashi, Phys. Rev. B **54**, 15849
(1996).

51 M. Matsuda, T. Yosihama, K. Kakurai, and G. Shirane, Phys. Rev. B **59**, 1060 (1999).
52 T. Fukuda, J. Mizuki, and M. Matsuda, Phys. Rev. B **66** (2002).
53 E. Dagotto and T. M. Rice, Science **271**, 618 (1996).
54 E. Dagotto, J. Riera, and D. Scalapino, Phys. Rev. B **45**, 5744 (1992).
55 C. Hess, C. Baumann, and B. Büchner, J. Magn. Magn. Mater. **290**, 322 (2005).
56 J. C. Bonner and H. W. J. Blöte, Phys. Rev. B **25**, 6959 (1982).
57 M. Montagnese, et al., Phys. Rev. Lett. **110**, 147206 (2013).
58 D. Merrill, D. Moore, S. Bauers, M. Falmbigl, and D. Johnson, Materials **8**, 2000 (2015).
59 M. Falmbigl, A. Fiedler, R. E. Atkins, S. F. Fischer, and D. C. Johnson, Nano Lett. **15**,
943 (2015).
60 R. Samnakay, D. Wickramaratne, T. R. Pope, R. K. Lake, T. T. Salguero, and A. A.
Balandin, Nano Lett. **15**, 2965 (2015).
61 C. Wan, Y. Wang, N. Wang, and K. Koumoto, Materials **3**, 2606 (2010).

Figures

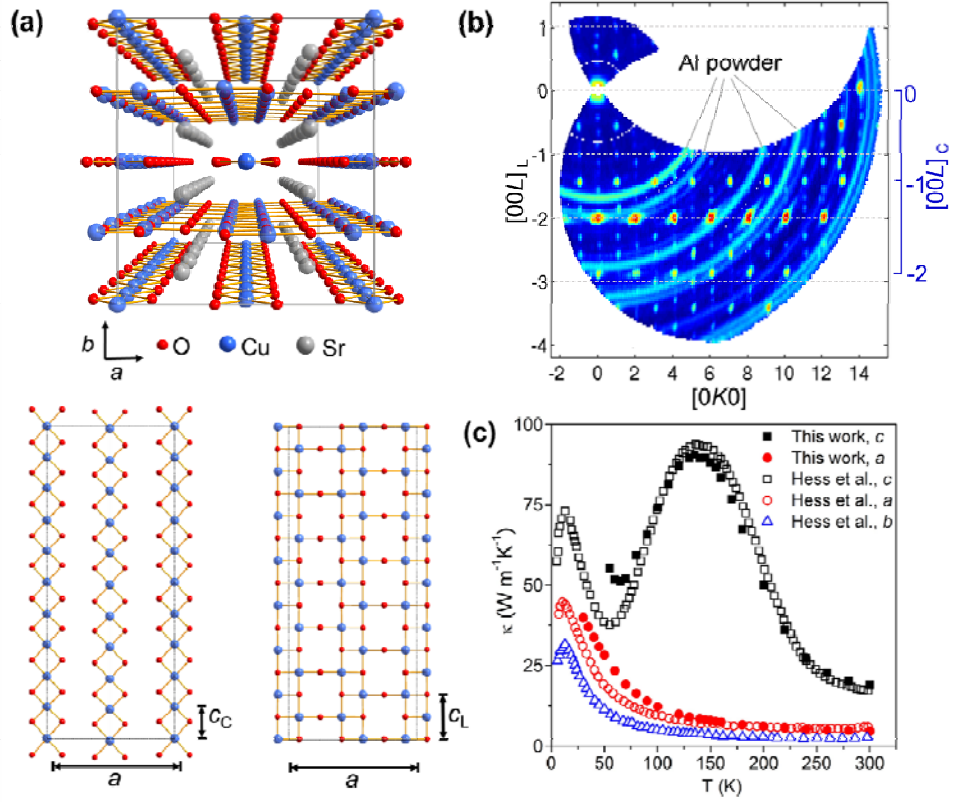


FIG. 1. (Color online) (a) Schematic illustrations of the crystal structure of $\text{Sr}_{14}\text{Cu}_{24}\text{O}_{41}$. (b) Reciprocal space map of elastic scattering from ARCS measurements with the incident neutron energy $E_i = 30$ meV at $T = 5$ K. (c) Thermal conductivity of $\text{Sr}_{14}\text{Cu}_{24}\text{O}_{41}$ single crystal along different axes measured in this work and reported by Hess *et al.*³⁸ The uncertainty of the thermal conductivity measurement of the present work is 15%.

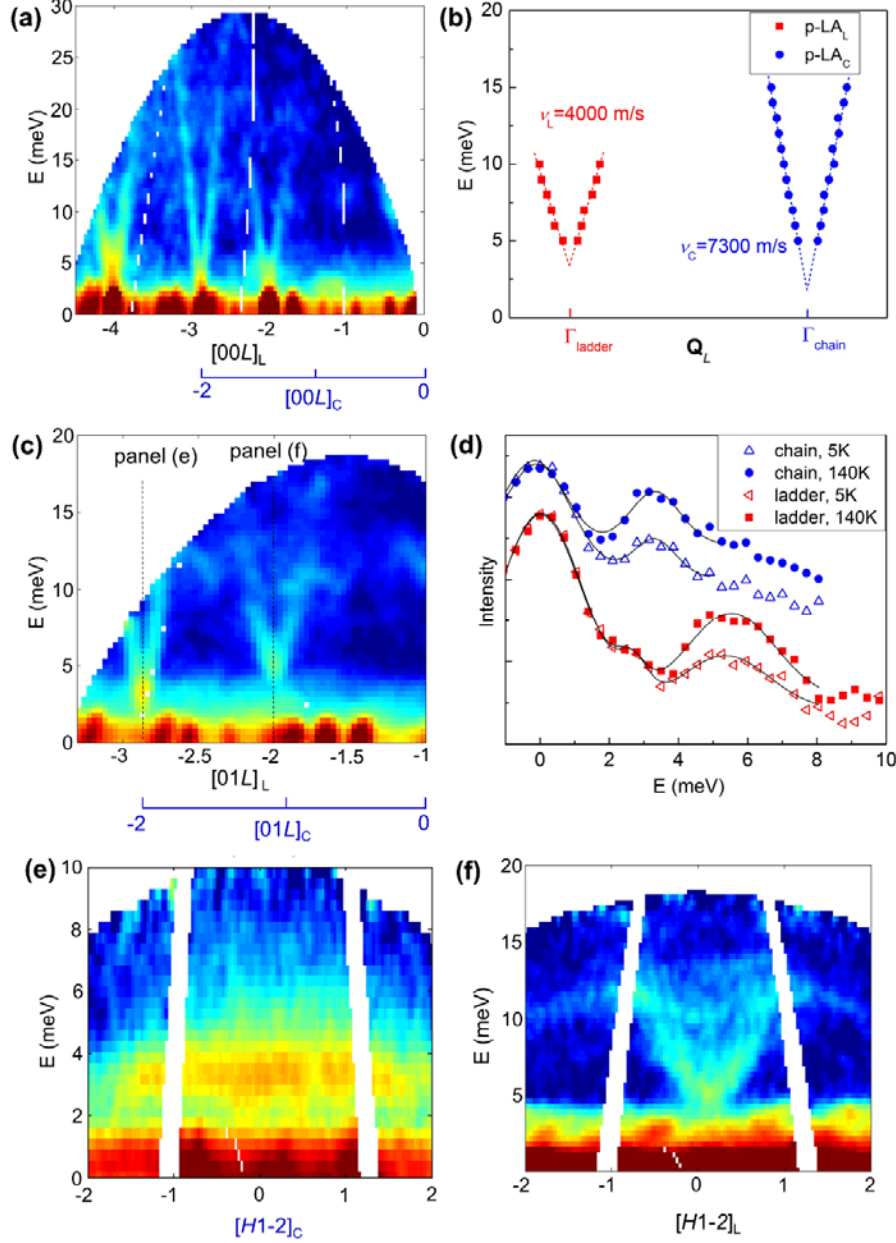


FIG. 2. (Color online) Measured INS signal of Sr₁₄Cu₂₄O₄₁ single crystal at 5 K showing the c -polarized acoustic-like modes. (a) $S(\mathbf{Q}, E)$ data along $[00L]_L$ with $E_i = 50$ meV showing the two sets of LA-like dispersions associated with the chain and ladder sublattices. (b) Peak values of $S(\mathbf{Q}, E)$ data of the two LA-like dispersions from (a). The dotted straight lines are linear fits of the measurement data, which extrapolate to small energy gaps at the zone center. (c) $S(\mathbf{Q}, E)$ data along $[01L]_L$ with $E_i = 30$ meV showing the energy gaps for the two LA-like dispersions. The dashed lines show the positions of the cuts in (e) and (f). (d) Energy-dependent INS intensities measured at a constant $\mathbf{Q} = (01-2)_L$ and $\mathbf{Q} = (01-2)_C$, respectively, at 5 K and 140 K. The solid lines are the peak fits of the measurement data. (e,f) $S(\mathbf{Q}, E)$ data along $[H1-2]_C$ and $[H1-2]_L$, respectively, with $E_i = 30$ meV.

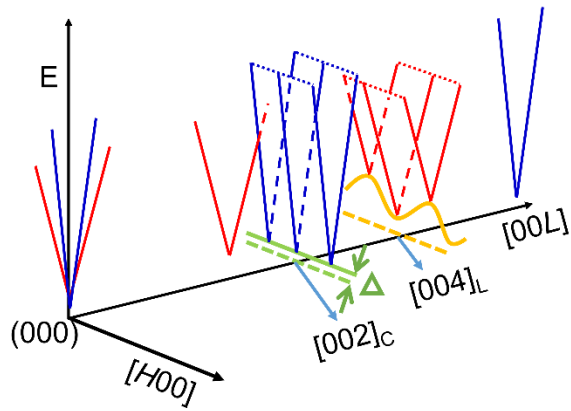


FIG. 3. (Color online) Schematic phonon dispersion relations in the $(H0L)$ plane for polarization parallel to the c axis. Portions of the dispersion surfaces for two LA-like phonons are indicated.

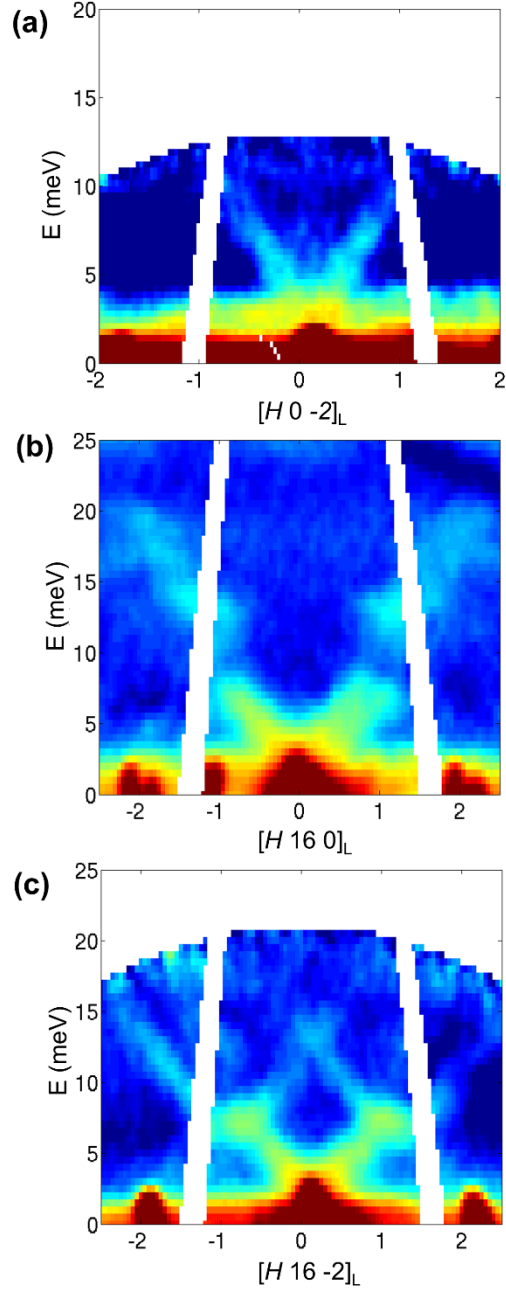


FIG. 4. (Color online) Measured INS signal of $\text{Sr}_{14}\text{Cu}_{24}\text{O}_{41}$ single crystal for wave vectors along a at 5 K. (a) $S(\mathbf{Q}, E)$ data along $[H 0 -2]_L$ with $E_i = 30$ meV showing the c -polarized TA-like mode. (b) $S(\mathbf{Q}, E)$ data along $[H 16 0]_L$ with $E_i = 50$ meV showing the b -polarized TA mode. (c) $S(\mathbf{Q}, E)$ data along $[H 16 -2]_L$ with $E_i = 50$ meV showing the low-energy optical modes.

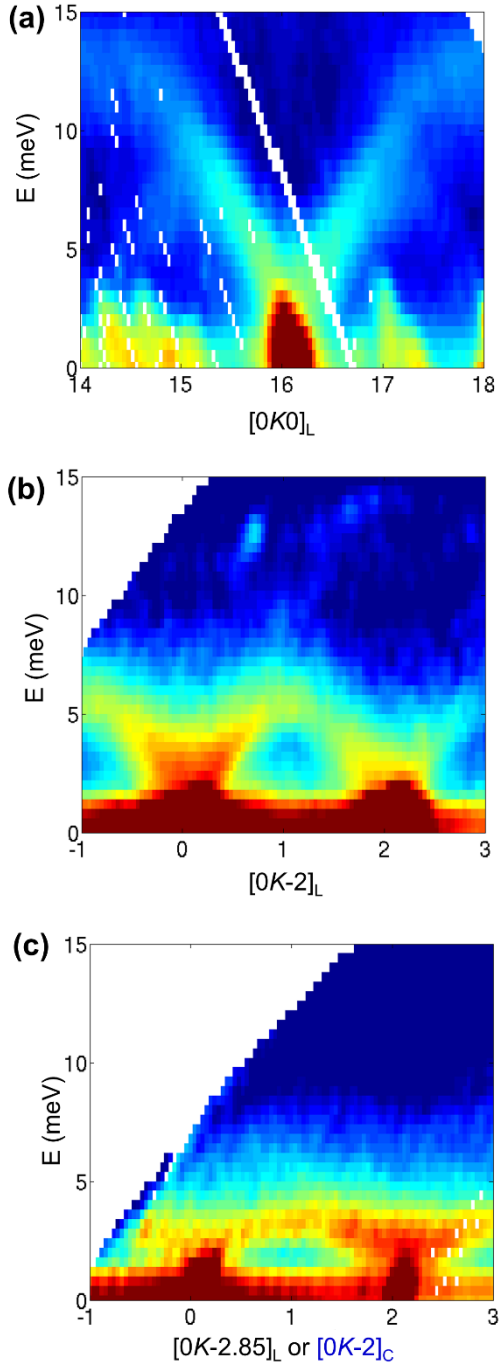


FIG. 5. (Color online) Measured INS signal of $\text{Sr}_{14}\text{Cu}_{24}\text{O}_{41}$ single crystal for wave vectors along b . (a) $S(\mathbf{Q}, E)$ data at 5 K along $[0K0]_L$ with $E_i = 50$ meV showing the LA mode. (b,c) $S(\mathbf{Q}, E)$ data at 140 K along $[0K-2]_L$ and along $[0K-2]_C$ with $E_i = 30$ meV showing the c -polarized TA-like modes associated with the ladder and chain sublattices, respectively.

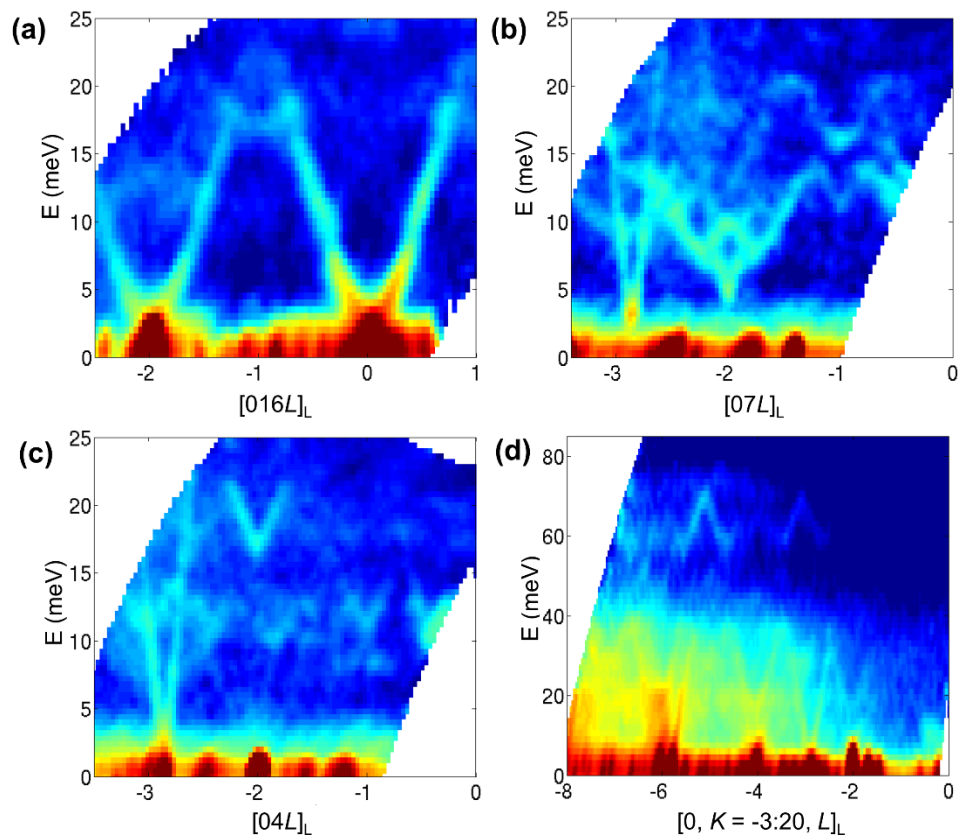


FIG. 6. (Color online) Measured INS signal of $\text{Sr}_{14}\text{Cu}_{24}\text{O}_{41}$ single crystal along c at 5 K showing the TA mode and optical modes. (a) $S(\mathbf{Q}, E)$ data along $[016L]_L$ with $E_i = 50$ meV showing the TA mode. (b,c) $S(\mathbf{Q}, E)$ data along $[07L]_L$ and $[04L]_L$ with $E_i = 30$ meV showing the low-lying optical modes as well as the LA modes of two sublattices. (d) $S(\mathbf{Q}, E)$ data obtained by integrating K from -3 to 20 with $E_i = 150$ meV, showing the high-energy optical modes.

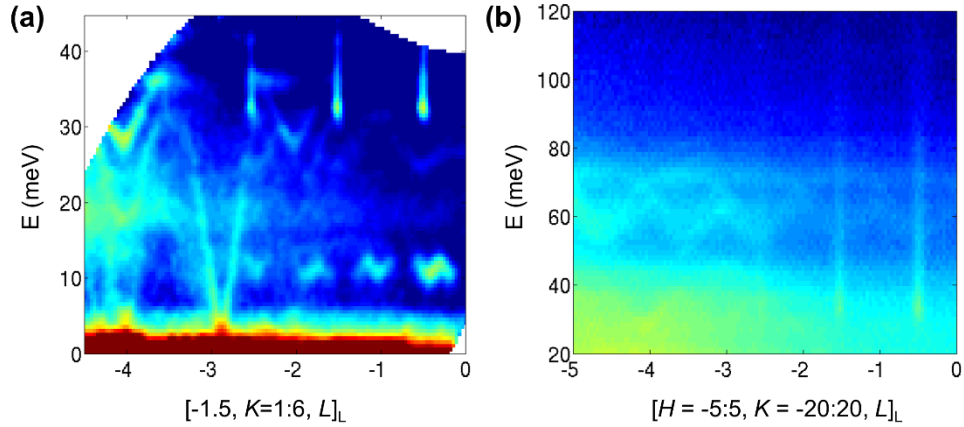


FIG. 7. (Color online) Measured INS signal of $\text{Sr}_{14}\text{Cu}_{24}\text{O}_{41}$ single crystal at 5 K showing the magnon dispersion of the ladders and phonon branches. (a) $S(\mathbf{Q}, E)$ data along c with $E_i = 50$ meV integrated from 1 to 6 in K , showing the spin-triplet dispersions from both the ladder and chain sublattices in addition to the LA-like mode for the chains and optical modes. (b) $S(\mathbf{Q}, E)$ data along c with $E_i = 150$ meV integrated from -5 to 5 in H and -20 to 20 in K showing the spin-triplet dispersion from the ladder sublattice and high-energy optical phonons.

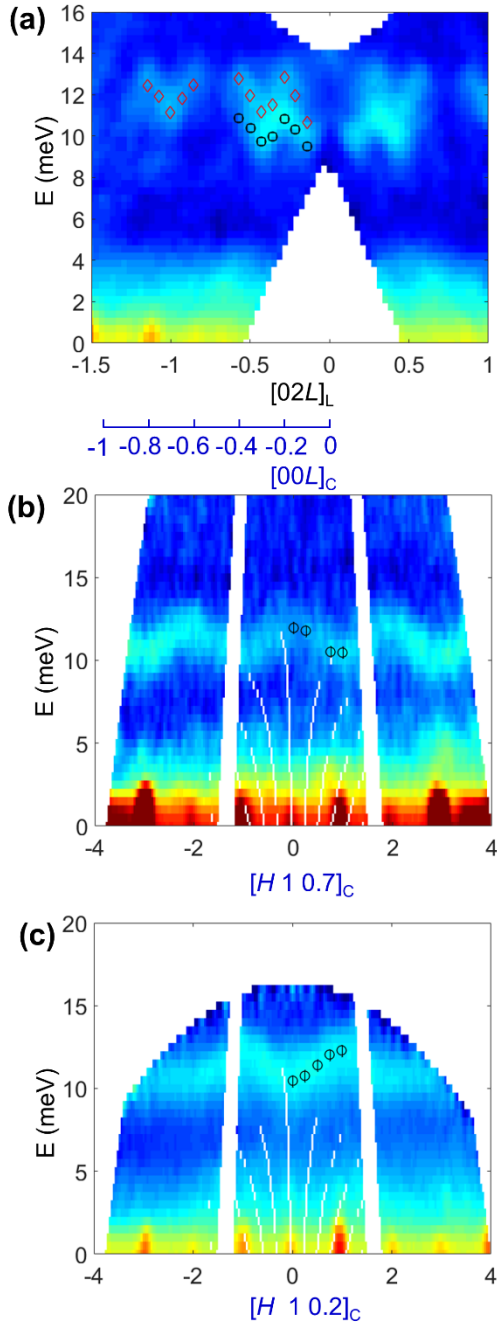


FIG. 8. (Color online) Measured INS signal of $\text{Sr}_{14}\text{Cu}_{24}\text{O}_{41}$ single crystal at 5 K showing the magnon dispersion of the chains. (a) $S(\mathbf{Q}, E)$ data along c with $E_i = 30$ meV showing the low-energy magnon dispersions. The open symbols are the INS results reported by Matsuda *et al.*⁵¹ (b,c) $S(\mathbf{Q}, E)$ data along a with $E_i = 50$ meV showing the two low-energy magnon dispersions. The open symbols are the INS results reported by Regnault *et al.*²⁷

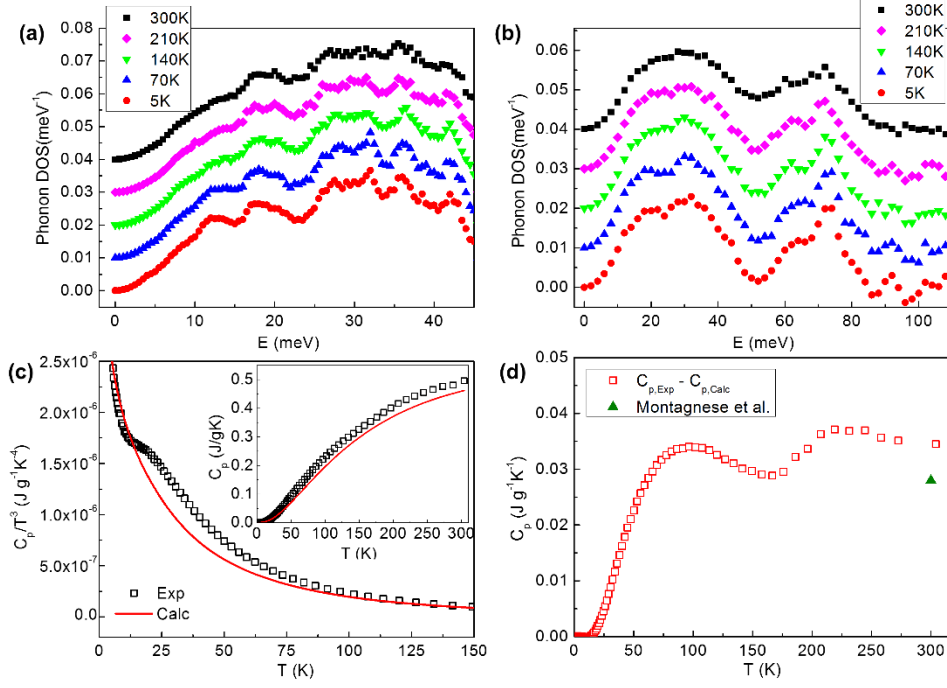


FIG. 9. (Color online) Neutron weighted phonon DOS of $\text{Sr}_{14}\text{Cu}_{24}\text{O}_{41}$ polycrystalline sample at different temperatures for incident neutron energies of (a) 50 meV and (b) 200 meV. (c) Temperature dependence of the measured and calculated specific heat data of $\text{Sr}_{14}\text{Cu}_{24}\text{O}_{41}$ in a $C_p(T)/T^3$ versus T plot. The inset of (c) is the $C_p(T)$ versus T plot. (d) The difference between $C_{p,\text{Exp}}$ and $C_{p,\text{Calc}}$ in comparison with the magnon specific heat calculated by Montagnese *et al.*⁵⁷

Table I. Group velocities of the acoustic and acoustic-like phonons along different axes based on the INS data compared to the sound velocities derived from resonant ultrasound spectroscopy⁴⁴.

Branch	INS ν_g (m s⁻¹)	ν_g (m s⁻¹) from Ref. ⁴⁴
[00L]		
LA	-	6430
LA _L	4000	-
LA _C	7300	-
<i>b</i> -TA	2100	-
[0K0]		
LA	3280	-
<i>c</i> -TA _L	2200	-
<i>c</i> -TA _C	1500	-
[H00]		
LA	-	6590
<i>b</i> -TA	3300	-
<i>c</i> -TA _L	3800	-
<i>c</i> -TA _C	~0	-
<i>c</i> -TA	-	3280